THE ASTROPHYSICAL JOURNAL, 547:292–301, 2001 January 20

A SHOCK-INDUCED PHOTODISSOCIATION REGION IN THE HH 80/81 FLOW: FAR-INFRARED SPECTROSCOPY[1]

SERGIO MOLINARI[2]
Infrared Processing and Analysis Center, California Institute of Technology, MS 100-22, Pasadena, CA 91125; molinari@ipac.caltech.edu
ALBERTO NORIEGA-CRESPO
SIRTF Science Center, California Institute of Technology, IPAC 100-22, Pasadena, California, 91125; alberto@ipac.caltech.edu
AND
LUIGI SPINOGLIO
CNR–Istituto di Fisica dello Spazio Interplanetario, via Fosso del Cavaliere I-00133 Rome, Italy; luigi@ifsi.rm.cnr.it
Received 2000 July 24; accepted 2000 August 25

ABSTRACT

The two spectrometers on board the *Infrared Space Observatory* were used to observe the Herbig-Haro objects HH 80, 81, and 80N, as well as their candidate exciting source IRAS 18162−2048. The fine structure lines of [O I] 63 μm, [O I] 145 μm, and [C II] 158 μm are detected everywhere, while [N II] 122 μm and [O III] 88.3 μm are only detected toward the HH objects; line ratios confirm for the first time the collisionally excited HH nature of HH 80N. No molecular line is detected in any of the observed positions. We use a full shock code to diagnose shock velocities $v_s \sim 100$ km s^{-1} toward the HH objects, as expected from the optical spectroscopy. Since proper motions suggest velocities in excess of 600 km s^{-1}, the HH objects probably represent the interface between two flow components with velocity differing by $\sim v_s$. Aside from the flow exciting source, the [C II] 158 μm line is everywhere brighter than the [O I] 63 μm line, indicating the presence of a photodissociation region (PDR) all along the flow. Continuum emission from the HH objects and from other positions along the flow is only detected longward of ~ 50 μm, and its proportionality to the [C II] 158 μm line flux suggests it is PDR in origin. We propose that the far-ultraviolet continuum irradiated by the HH objects and the jet is responsible for the generation of a PDR at the walls of the flow cavity. We develop a very simple model which strengthens the plausibility of this hypothesis.

Subject headings: infrared: ISM: lines and bands — ISM: Herbig-Haro objects — ISM: individual (HH 80–81) — ISM: jets and outflows — stars: formation

1. INTRODUCTION

Stellar jets and outflows arising from low-mass protostellar objects are considered ubiquitous, since essentially each protostar must go through an active period of mass loss to get rid of its angular momentum to become a star (cf. Hartmann 1998). These outflows are well collimated and supersonic and interact mostly through shocks with the interstellar medium. When these shock-excited regions are detected by optical means, they are identified as Herbig-Haro objects (Reipurth & Heathcote 1997).

The process of mass loss for intermediate- and high-mass protostellar objects is less well understood (Churchwell 1999). Observationally, very few of these objects have collimated optical jets or well-defined molecular outflows (Poetzel, Mundt, & Ray 1989; Shepherd & Churchwell 1996). The Herbig-Haro 80/81 system, which is driven by a 20,000 $L_\odot$ *IRAS* source, is one of those rare cases with a well-collimated supersonic jet that reaches flow velocities of $\sim$600–1400 km s^{-1} (Martí, Rodríguez, & Reipurth 1995, 1998). HH 80/81 are at the edge of the L291 cloud in Sagittarius (Reipurth & Graham 1988) at an estimated kinematical distance of 1.7 kpc (Rodríguez et al. 1980). At this distance the HH 80/81 system, with an angular size of $\sim 10\farcm8$, spans $\sim$5.3 pc. The proper-motion measurements confirm that IRAS 18162−2048 is the source driving the outflow, which is part of a small cluster of infrared sources (Aspin & Geballe 1992; Aspin et al. 1994). IRAS 18162−2048, given its large luminosity, is likely to become a B-type star. Most of the early work on HH 80/81 was performed at radio wavelengths, where 3.6 and 6 cm observations found the collimated radio jet emanating from IRAS 18162−2048, as well as a section of the counterflow, named HH 80N, which is optically invisible (Rodríguez & Reipurth 1989; Martí, Rodríguez, & Reipurth 1993, hereafter MRR93).

Recently, Heathcote, Reipurth, & Raga (1998, hereafter HRR) have carried a detailed analysis of HH 80/81 morphology and kinematics, using *Hubble Space Telescope* WFPC2 images and ground-based optical images and spectra. They concluded in their study that the emission arising from HH 80/81 is due to shocks with velocities up to 600 km s^{-1}. The energy release by such shocks is so high that it thermalizes the gas to temperatures greater than 10^6 K, i.e., the shocks are adiabatic. If the HH objects were to resemble bow shock structures (Raga & Böhm 1986; Hartigan, Raymond, & Hartmann 1987), then the optical emission observed in Hα or [O III] λ5007 comes from the "wings," while the stagnation region (the tip of the bow) is

[1] Based on observations with *ISO*, an ESA project with instruments funded by ESA Member States (especially the PI countries: France, Germany, the Netherlands, and the United Kingdom) with the participation of ISAS and NASA.

[2] Present address: Instituto di Fisica dello Spazio Interplanetario, via Fosso del Cavaliere, I-00133 Rome, Italy; molinari@ifsi.rm.cnr.it.

TABLE 1

OBSERVATIONS

Object	Position	α (B1950)	δ (B1950)	AOTs and TDTs
IRAS 18162−2048......	ON	18 16 12.9	−20 48 49	LWS01-32901362
	OFF S	18 16 12.9	−20 50 29	LWS01-32901362
	OFF N	18 16 12.9	−20 47 09	LWS01-32901362
HH 80....................		18 16 06.8	−20 53 06	LWS01-32901350, SWS01-32901351
HH 81....................		18 16 07.4	−20 52 23	LWS01-32901360, SWS01-32901361
HH 80N		18 16 20.7	−20 42 53	LWS01-32901363

NOTE.—Units of right ascension are hours, minutes, and seconds, and units of declination are degrees, arcminutes, and arcseconds.

several times farther ahead and invisible. This scenario, however, is derived by modeling the optical line profiles (HRR); from the morphological viewpoint, the HH objects appear as irregular knots that do not resemble wings of a bow.

In this study we present *Infrared Space Observatory* (*ISO*) (Kessler et al. 1996) spectroscopic observations of the HH 80/81/80N system, including their exciting source IRAS 18162−2048. The observations and data analysis are presented in § 2 and the results in § 3. A model to interpret the results is presented in § 4 and discussed in § 5. We summarize our conclusions in § 6.

2. OBSERVATIONS

We used the two spectrometers on the *ISO* satellite to observe several locations along the HH 80/81 flow, including the candidate exciting source IRAS 18162−2048. The Long Wavelength Spectrometer (LWS) (Clegg et al. 1996) was used in its LWS01 grating mode to acquire full low-resolution ($R \sim 200$) 43–197 μm scans. Data were collected every 1/4 of a resolution element (equivalent to ~ 0.07 μm for $\lambda \lesssim 90$ μm and to ~ 0.15 μm for $\lambda \gtrsim 90$ μm) with 0.5 s integration time; a total of 24 scans were accumulated, corresponding to 48 s integration time per spectral element. LWS data processed through Off-Line Processing (OLP), version 7, have been reduced using the LWS Interactive Analysis (LIA) version 7.2.[3] The dark current and gain for each detector were reestimated, and the data were recalibrated in wavelength, bandpass, and flux. The absolute flux calibration for LWS in grating mode is 10% (*ISO* Handbook, IV, 4.3.2).[4]

The Short Wavelength Spectrometer (SWS) (de Graauw et al. 1996) was used in its SWS01 "Speed 2" grating mode. In this mode the grating is moved faster than the detector reset time, with a loss of about a factor 7 (*ISO* Handbook, VI, 3.3) in achievable spectral resolution, resulting in $R \sim 300$. The total observing time was about 1900 s. SWS data were processed using OSIA, the SWS Interactive Analysis.[5] Dark currents and photometric checks were revised. The 1998 March bandpass calibration files have been used to produce the final spectra. The accuracy of the SWS absolute flux calibration varies between 7% and 35% from 2 to 40 μm (*ISO* Handbook, VI, 5.4.2).

The final steps of data analysis were done using the *ISO* Spectral Analysis Package[6] (ISAP) version 1.6a for both LWS and SWS. Grating scans (LWS) and detectors spectra (SWS) were averaged using a median clipping algorithm optimized to flag and discard outliers mainly due to transients. The LWS spectra were heavily fringed, and standard techniques available under ISAP were used to remove these instrumental effects. Line fluxes were estimated by means of Gaussian fitting.

Table 1 lists the observed positions, which are also reported in Figure 1 as the centers of the dashed circles (the LWS FWHM beam size) superimposed on the 6 cm Very Large Array (VLA) map of MRR93. The last column

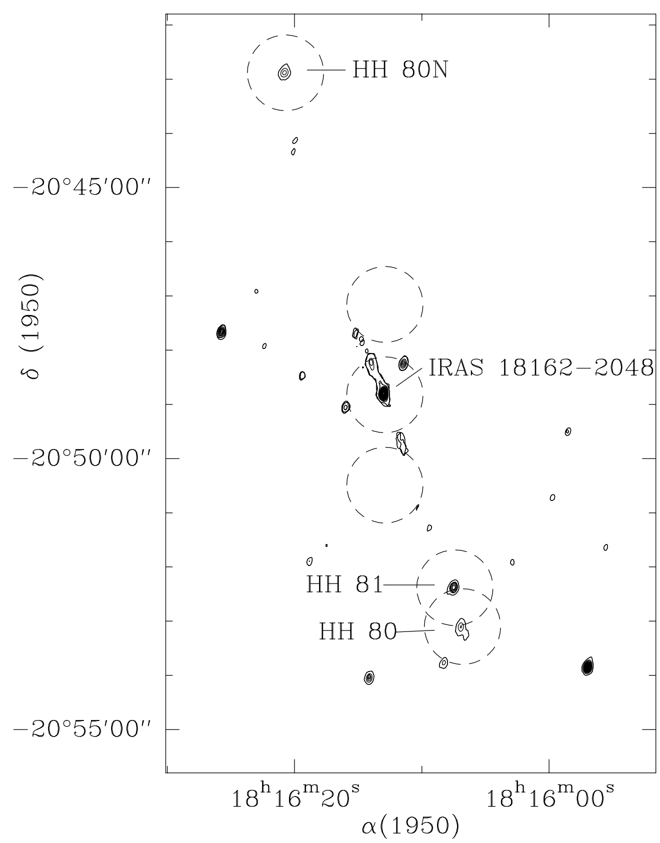

FIG. 1.—VLA 6 cm composite map of the HH 80/81 region (Martí et al. 1993, courtesy of L. F. Rodríguez); superimposed is the *ISO*-LWS field of view (*dashed circles*) at all observed positions. The various sources in the field are labeled.

[3] LIA is available at http://www.ipac.caltech.edu/iso/lws/lia/lia.html.

[4] *ISO* Handbook, http://www.iso.vilspa.esa.es/users/handbook/.

[5] OSIA is available at http://www.mpe.mpg.de/www_ir/ISO/observer/osia/osia.html.

[6] ISAP is available at http://www.ipac.caltech.edu/iso/isap/isap.html.

reports the Astronomical Observation Template (AOT) used, together with the eight-digit unique identifier of the observation (TDT).

3. RESULTS

All objects were detected with the LWS, while no line or continuum is detected with the SWS toward HH 80 and 81. Table 2 lists the measured fluxes for the detected lines; upper limits are given at the 1 σ level. The distance between HH 80 and 81 is about $\frac{1}{2}$ of the LWS beam size ($\sim 80''$ FWHM at most wavelengths; see *ISO* Handbook, IV, 4.10.1) implying that each object contributes roughly half of its flux (lines and continuum) to the observed flux of its neighbor. Contamination-corrected fluxes for HH 80 and 81 are listed just below the observed ones for each line.

A glance at Table 2 is sufficient to identify the basic results of our observations and set the guidelines for the interpretation of our data. First of all we note that the [N II] 122 μm and [O III] 88.3 μm lines are only detected toward the HH objects; these observations provide the first direct evidence for the collisionally excited HH nature of HH 80N. Although the LWS pointing toward IRAS 18162−2048 encompasses the radio-brightest portions of the thermal jet, no lines from ionized species (other than [C II] 158 μm, but see below) are detected. We verified that the [N II] 122 μm and [O III] 88.3 μm lines detected toward the HH objects would still be detectable toward IRAS 18162−2048, in spite of the higher photon noise from this more intense continuum source. Second, molecular emission is not detected anywhere. Finally, we note that with the exception of IRAS 18162−2048 the [C II] 158 μm line is everywhere brighter than the [O I] 63 μm line. The detected lines are reported in Figure 2 for the HH object pointings and in Figure 3 for the three central observed positions of the flow.

3.1. *The Herbig-Haro Objects*

The HH 80/81 system is the most powerful flow known to emanate from an intermediate-mass young stellar object (YSO). Velocities in excess of 600 km s^{-1} are derived from proper motion measurements both in radio continuum (Martí et al. 1995, 1998) and optical lines (HRR). In addition, line profile analysis of high-dispersion optical spectra suggests shock velocities $v_s \sim 650$ km s^{-1} (HRR). Interestingly enough, however, optical spectra only reveal lines from species up to double ionization state. Our far-infrared (FIR) spectroscopy has the immediate advantage that reddening corrections, which are critical in the optical regime especially in this highly extincted region (HRR), are not important. To diagnose the shock conditions toward HH 80, 81 and 80N, we compare our observations with the predictions from plane-parallel atomic shock models. The shock models were calculated using MAPPINGS2, a code developed by Binette, Dopita, & Tuohy (1985), which has been thoroughly tested (Pequignot 1986).

A grid of models was created changing the preshock density between 10^2 and 10^4 cm^{-3}, consistent with values derived by HRR from optical-line analysis. Shock velocities were varied between 60 and 110 km s^{-1}; higher values, although still compatible with results from optical line ratios (HRR), fail to produce lines like [N II] 122 μm and [O III] 88.3 μm which are instead observed toward the HH objects. The preshock degree of ionization and magnetic field strength were kept fixed at 0.1 and 10 μG, respectively. These values are not critical for the velocities we used (but see HRR's § 8.2) and represent typical values for stellar jets (but see Bacciotti & Eislöffel 1999) from low-mass YSOs; we will assume they are also valid for higher mass systems like the one we are presently dealing with. This selection of initial values also allows us to gauge our models with those of Hartigan et al. (1987). In all instances solar abundances were used, since this is a reasonable assumption for Herbig-Haro objects (Beck-Winchatz, Böhm, & Noriega-Crespo 1996).

Figure 4 clearly shows that shock velocities between 90 and 110 km s^{-1} are appropriate to reproduce the emitted spectra for all HH objects. Preshock densities between 100 and 1000 cm^{-3} are derived, in full agreement with estimates from HRR. In these conditions of low-density J-shocks (Draine 1980), negligible cooling is expected from molecular lines like CO, H_2, and H_2O (Hollenbach & McKee 1989), in agreement with our observations. Furthermore, the absence of far-infrared (FIR) molecular emission also rules out the presence of a significant C-type shock component, for which H_2, CO, and H_2O molecular lines would be the main coolants (e.g., Kaufman & Neufeld 1996).

These low-velocity shocks plus the width of the observed optical lines suggested to HRR that the HH 80/81 objects correspond to "wings" of a highly adiabatic bow shock

TABLE 2

Observed Line Fluxes

Line	IRAS 18162−2048 ON	IRAS 18162−2048 OFF S	IRAS 18162−2048 OFF N	HH 80	HH 81	HH 80N
[O I] 63 μm	104 (2)	7.1 (0.5)	8.0 (0.3)	6.4 (0.2)	7.1 (1.0)	8.2 (0.2)
				3.8[a]	5.2[a]	
[O I] 145 μm	10.6 (0.7)	0.3 (0.1)	1.0 (0.2)	0.4 (0.1)	0.32 (0.04)	0.7 (0.2)
				0.3[a]	0.16[a]	
[O III] 88.3 μm	≤ 4	≤ 0.3	≤ 0.4	0.8 (0.4)	1.0 (0.4)	1.0 (0.2)
				0.4[a]	0.8[a]	
[N II] 122 μm	≤ 1	≤ 0.3	≤ 0.2	0.35 (0.08)	0.53 (0.07)	0.7 (0.1)
				0.11[a]	0.47[a]	
[C II] 158 μm	37 (1)	16.3 (0.3)	20.4 (0.3)	11.49 (0.06)	12.53 (0.08)	17.1 (0.1)
				6.97[a]	9.04[a]	

Note.—Units of 10^{-19} W cm^{-2} and 1 σ statistical uncertainties in parenthesis; upper limits are at the 1 σ level.

[a] Contamination-corrected fluxes.

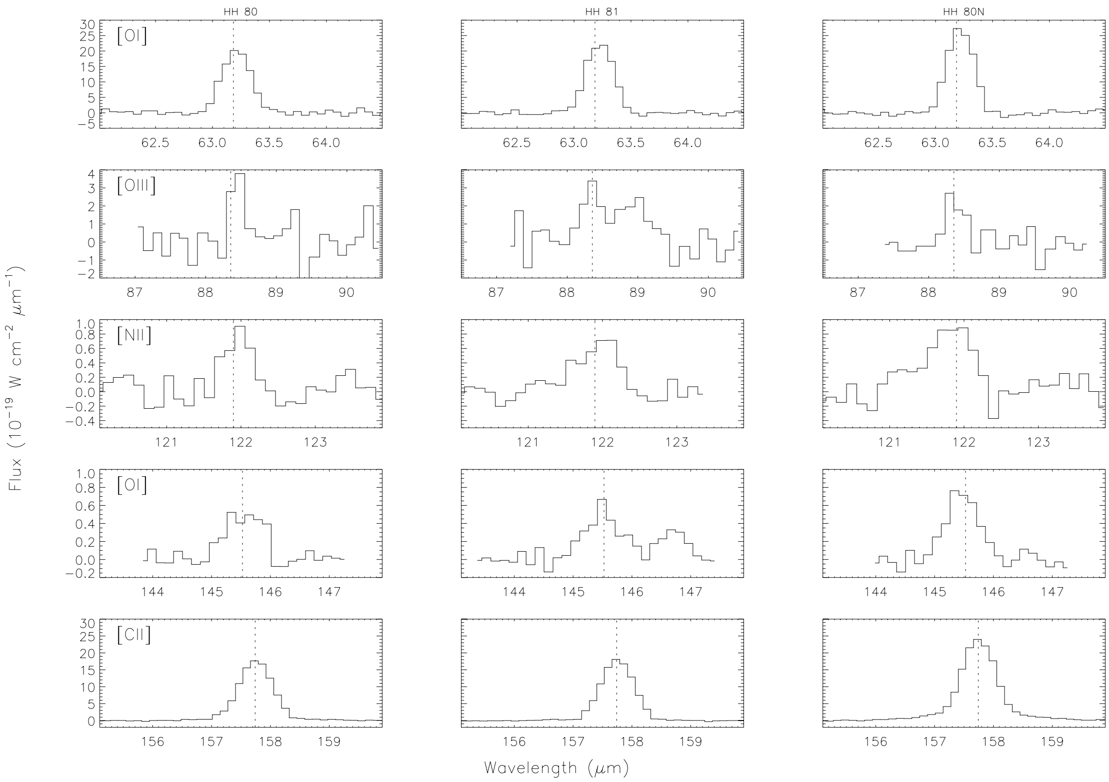

FIG. 2.—Detected lines toward HH 80, 81, and 80N. Flux densities are normalized to 10^{-19} W cm^{-2} μm^{-1}. The dotted vertical lines represent the expected line center wavelength.

that strikes the surrounding gas at $\sim$650 km s^{-1}; in such wings the shock front would be oblique with respect to the direction of motion, resulting in lower shock velocities. A shock velocity of $\sim$100 km s^{-1} and flow velocities (from the proper motions) as high as 600 km s^{-1} can also be reconciled if one considers that the mass loss from the protostar is time dependent, and that the observed configuration of HH 80/81 was preceded by previous ejection events. If this is the case, the new ejected gas finds the circumstellar gas already in motion, and it is the interaction between these two flows that can create relative shock velocities of $\sim$100 km s^{-1} or so (Raga et al. 1990; Stone & Norman 1993). Multiepoch VLA observations (Martí et al. 1995, 1998) of the jet's radio knots provide supporting evidence for episodic mass loss from IRAS 18162$-$2048.

A similar process has been invoked to understand the flow characteristics of the HH 1/2 system, where the proper motions are as high as 450 km s^{-1} in both atomic and molecular H_2 gas (Herbig & Jones 1981; Rodríguez et al. 1990; Eislöffel, Mundt, & Böhm 1994; Noriega-Crespo et al. 1997), but the shocks themselves are $\sim$150–200 km s^{-1} (Hartigan et al. 1987; Noriega-Crespo, Böhm, & Raga 1990). In the HH 1/2 outflow, however, there is clear evidence of a previous outburst event marked by the presence

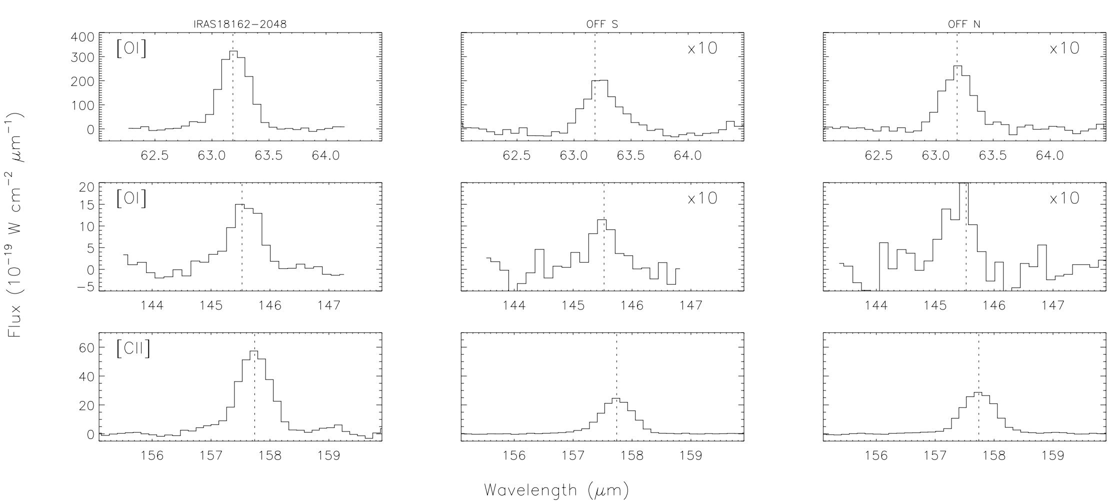

FIG. 3.—Detected lines toward IRAS 18162$-$2048, OFF S and OFF N. Flux densities are normalized to 10^{-19} W cm^{-2} μm^{-1}. The dotted vertical lines represent the expected line center wavelength.

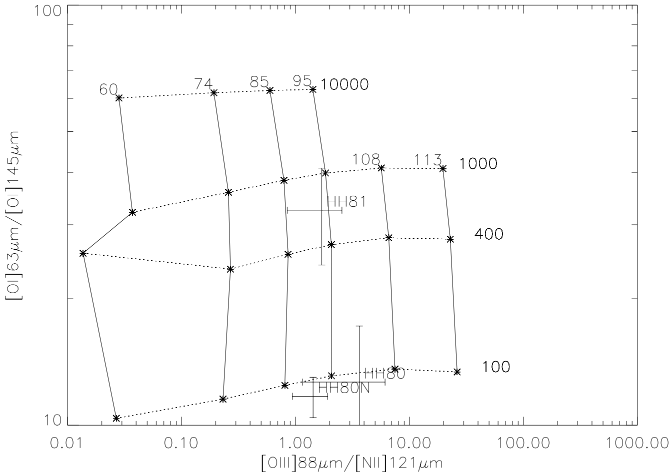

FIG. 4.—[O I] 63 μm/[O I] 145 μm vs. [O III] 88.3 μm/[N II] 122 μm diagnostic diagram obtained from the models of Binette et al. (1985). Horizontal lines are of constant preshock density (in cm^{-3}), while vertical lines are of constant shock velocity (in km s^{-1}).

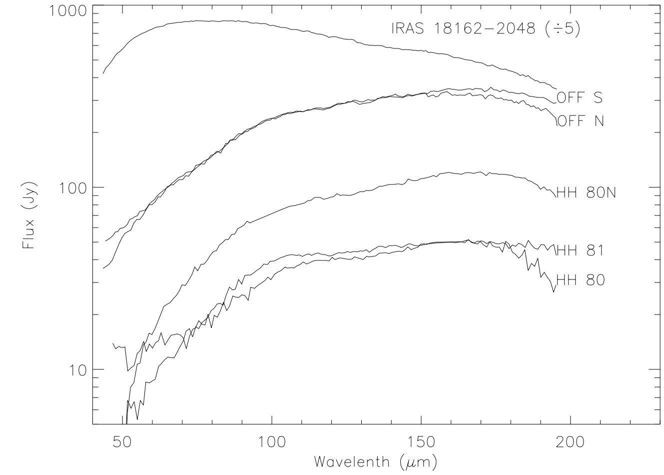

FIG. 5.—Spectral energy distributions observed with LWS toward all pointings. The SED from IRAS 18162−2048 has been divided by 5 to fit it into the plot range. The SEDs of HH 80 and 81 have been corrected for reciprocal contamination.

of an older bow shock structure ∼10 times farther away from central outflow source (Ogura 1995).

3.2. *The Jet*

The LWS pointing toward IRAS 18162−2048 encompasses the base of the radio thermal jet, which is the strongest radio emitter in the flow. Yet no [O III] 88.3 μm or [N II] 122 μm emission is detected, indicating that the ionized material of the jet is at a lower temperature compared to HH 80, 81, and 80N or that the ionization does not result from shocks. Interestingly, the radio spectral index of the jet is consistent with that of an ionized wind but significantly differs from that of the HH objects which instead manifest a possible synchrotron component (MRR93). This behavior is different from that of the HH 1/2 system, for instance, where the central source VLA 1 (Pravdo et al. 1985) has a similar positive radio spectral index to that of HH 80/81 jet, but for the HH objects themselves it is flat, indicating optically thin free-free emission (Rodríguez et al. 1990).

3.3. *The PDR*

In the shock conditions diagnosed by our FIR spectroscopy (see § 3.1), [C II] 158 μm contributes about 20% of the [O I] 63 μm cooling. Since [C II] 158 μm is everywhere brighter than [O I] 63 μm (except toward IRAS 18162−2048), the [C II] 158 μm emission must have another origin, namely, PDR. Evidence for a PDR-like emission is also offered by the FIR continua detected toward the HH object and the OFF positions (the latter cannot be entirely justified with contamination by the stronger continuum source IRAS 18162−2048).

Figure 5 shows the spectral energy distributions (SEDs) observed toward all pointed positions with the LWS. We note that the continuum observed toward the two OFF positions cannot be justified with contamination from IRAS 18162−2048. The continua from HH 80 and 81 have been corrected for reciprocal contamination (see end of § 2), and detector spectra have been stitched for cosmetic purposes.

In a PDR, electrons are released in the gas phase by far-ultraviolet (FUV)-irradiated dust grains via the photoelectric effect and heat the gas (Tielens & Hollenbach 1985). Theory and observations generally agree on the fact that between 0.1% and 1% of the incident FUV flux is converted into gas heating via this mechanism, and subsequently released mainly via "cooling" of the [C II] 158 μm line. The rest of the incident field is absorbed by dust and reprocessed to FIR wavelengths. We see from Figure 5 that the observed SEDs contain the bulk of FIR emission, so that their integral is a good representation of the reprocessed FUV field; the ratio of observed [C II] 158 μm to the integrated SEDs yields values $0.002 \leq \chi_c \leq 0.013$, in very good agreement with expectations for a PDR. The only obvious exception is IRAS 18162−2048, whose SED is dominated by radiation from the central YSO.

Assuming that the preshock densities diagnosed for the HH objects (§ 3.1) represent the average conditions surrounding the HH 80/81 flow, we can use the observed [C II] 158 μm flux to estimate the intensity of the irradiating FUV field. Using the Web Infrared Tool Shed[7] and assuming complete filling of the LWS beam with filling factor of unity, we estimate $G_0 \sim 200$, 400, 30,000, 200, 40, and 30 for the six LWS pointings from north to south (see Fig. 1), where G_0 is the FUV field intensity expressed in units of 1.6×10^{-3} ergs cm^{-2} s^{-1} (Habing 1968). In these conditions the PDR emission could account for most of the [O I] 63 μm and [O I] 145 μm fluxes everywhere along the flow, including the HH objects. In this case the [O I] 63 μm/[O I] 145 μm ratios would imply densities $n < 10^4$ cm^{-3}.

We searched several degrees around the HH 80/81 area for OB stars which could be responsible for this irradiation level, finding none. An obvious candidate is of course IRAS 18162−2048 itself. Assuming a B0 zero-age main-sequence spectral class (MRR93), the resulting FUV field at the various LWS pointings would be $G_0 \sim 450$ at OFF-N and OFF-S and ∼60 at the HH objects; the agreement with the G_0 values estimated from the [C II] 158 μm line can be considered satisfactory. *K*-band images of IRAS 18162−2048, however, clearly resolve the IRAS source in a small cluster of at least three sources (Aspin et al. 1994); redistribution of the total bolometric luminosity of the IRAS source among the cluster members, adopting the

[7] M. G. Wolfire, M. W. Pound, L. Mundy, & S. D. Lord. 2000, http://wits.ipac.caltech.edu.

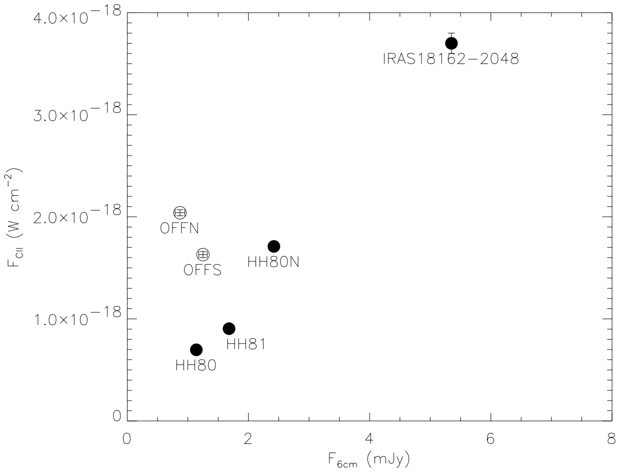

FIG. 6.—Plot of the [C II] 158 μm line flux vs. the 6 cm continuum flux from the knots of the jet encompassed by the LWS beam. When error bars are not visible it is because they are smaller than the symbols.

initial mass function from Miller & Scalo (1979), would assign only half of this luminosity to the most massive member of the cloud (e.g., Molinari et al. 2000 and references therein). This decreases the Lyman continuum photon flux by more than 1 order of magnitude and reduces G_0 by nearly 2 orders of magnitude, ruling out IRAS 18162−2048 as the PDR illuminating source.

An intriguing possibility is that the illuminating sources for the observed PDR emission are the HH objects and the jet. In Figure 6 we report the [C II] 158 μm line flux as a function of the 6 cm flux measured by MRR93. The filled symbols represent the HH objects and IRAS 18162−2048; for each object we consider the radio knots encompassed by the LWS beam at each position. The correlation between $F_{\rm C\,II}$ and $F_{\rm 6\,cm}$ would seem to suggest that the ionized material and the amount of cooling by the PDR may be somehow related. We note that the two OFF positions do not fit with the correlation in Figure 6. In the next paragraph we will propose a semiempirical model to verify and quantify the radio-PDR connection.

4. A MODEL FOR THE SHOCK/JET-PDR CONNECTION

The influence of shock-originated radiation on the surrounding medium in HH flows is not clear. NH_3 and HCO^+ enhancements have been detected in the vicinity of HH 80N, HH 1, and HH 2 (Girart et al. 1994; Girart, Estalella, & Ho 1998; Davis, Dent, & Burnell 1990; Torrelles et al. 1992, 1993), and it has been suggested that the UV field generated in the HH shocks may be responsible. Wolfire & Königl (1993), and more recently Raga & Williams (2000), have shown that the chemistry of blobs in the vicinity of HH objects can be influenced by the passage of the HH object, although the predicted morphologies do not match the observations.

We propose a scenario where the ionized material which is recombining behind the shock front and in the jet, and which emits free-free radio continuum, is also responsible for a UV field which illuminates internally the walls of the flow cavity; a PDR is there produced, which mainly cools via the [C II] 158 μm line. If this is correct, then we should be able to express the two observables, i.e., the radio continuum flux and the [C II] 158 μm line flux, as a function of a set of physical parameters which characterize the HH shocks, the jet, and the PDR.

Radio emission from shocked material has been modeled by Curiel, Cantó, & Rodríguez (1987); in the optically thin regime, the free-free emission from the recombination region can be written as

$$S_{\rm sh_\nu} = 1.84 \times 10^{-4}\theta^2\left(\frac{\nu}{10\ \rm GHz}\right)^{-0.1} T_4^{0.45}\, n_{0_{10}} v_{s_7} \times (1 + 3.483 v_{s_7} - 2.745)\ \rm mJy\ , \qquad (1)$$

where θ is the angular diameter in arcseconds of the recombination region, T_4 is the electron temperature in units of 10^4 K, $n_{0_{10}}$ is the preshock density in units of 10 cm^{-3}, and v_{s_7} is the shock velocity in units of 100 km s^{-1}. This model applies to HH 80, 80N, and 81, whose high-ionization lines clearly trace a high-velocity shock. In the absence of similar evidence toward the central source and the two OFF positions (Table 2), where the LWS beam encompasses most of the jet radio knots, we will assume that the ionization does not result from shocks. Reynolds (1986) developed a model to predict the properties of radio continuum emission from a collimated, ionized thermal jet. His expression of the radio flux at any specific frequency is a complicated function of jet parameters like the collimation, the density, temperature and ionization radial gradients, the initial distance where the jet is injected, the jet's width at its base. Because we cannot independently fix any of these parameters, the diagnostic power of this model will be very limited in the present case.

Let us now quantify the energy released by the shock recombination region, in the portion of the UV continuum, between 912 and 2066 Å (or between 13.6 and 6 eV), which is effective in PDR illumination. It is widely accepted (Dopita, Binette, & Schwartz 1982) that the dominant contribution to UV continuum in this wavelength range comes from hydrogenic $2s \rightarrow 1s$ two-photon decay. Theoretical models (Shull & McKee 1979, also confirmed by our grid of computed shock models; § 3.1) suggest that two-photon emission from He^0 and He^+ can be neglected in comparison. The H^0 two-photon emissivity is given by

$$j_\nu = \frac{1}{4\pi}\frac{h\nu}{\nu_0} P_{\nu/\nu_0} N_{2s}\ \rm ergs\ s^{-1}\ sr^{-1}\ cm^{-3}\ Hz^{-1}\ , \qquad (2)$$

where ν_0 is the Lyα frequency; P_{ν/ν_0} is the probability, symmetrical around $0.5\nu_0$, that a photon is emitted with frequency ν/ν_0 and for which we adopted the analytical approximation of Nussbaumer & Schmutz (1984); N_{2s} is the population density of level $2s$ and can be found equating the recombination rate from higher states to $2s$, with the total $2s \rightarrow 1s$ two-photon decay rate. We obtain (Emerson 1996)

$$N_{2s} \sim 0.3\alpha'_{\rm rec} N_e N_i A_{2q}^{-1}\ \rm cm^{-3}\ , \qquad (3)$$

where N_e and N_i are the electron and ion number densities and $A_{2q} \sim 8.23$ s^{-1} is the two-photon transition probability. The total recombination coefficient to all hydrogen excited levels can be written as (Hummer & Seaton 1963)

$$\alpha'_{\rm rec} = 1.627 \times 10^{-13} T_4^{-1/2} \times (1 - 1.657 \log_{10} T_4 + 0.584 T_4^{1/3})\ \rm cm^3\ s^{-1}\ , \qquad (4)$$

where T_4 is $T/10^4$ K. Using equations (2), (3), and (4), we are able to write the power radiated by the recombination region in the FUV as

$$L_{\rm FUV} = 4\pi V_{\rm rec}\,\eta_{\rm ce}\int_{6\ \rm eV}^{13.6\ \rm eV} j_\nu\,d\nu \ {\rm ergs\ s^{-1}}\ . \qquad (5)$$

Here $V_{\rm rec}$ is the volume of the recombination region, while $\eta_{\rm ce}$ is a factor which accounts for a collisional enhancement of the $2s$ level population above the values predicted by pure recombination. Such an enhancement can be determined from a comparison of the predicted two-photon spectrum with the observed UV continuum from HH objects. Dopita et al. (1982) find values $2.8 \le \eta_{\rm ce} \le 13.3$; interestingly, $\eta_{\rm ce}$ is found to be inversely proportional to the degree of excitation of the HH object as measured, e.g., from the [O III] λ5007/[O I] λ6300 ratio. Equation (5) makes the implicit assumption that the ionized clump is optically thin to the FUV radiation. It is easy to show that for typical dust grains of radius 0.1 μm and density of 3 g cm^{-3} the optical depth along the diameter of a spherical clump of radius r and particle density n can be written as

$$\tau_\nu = 1.8\times10^{-8} Q_\nu\, n r d\ , \qquad (6)$$

where n is in cm^{-3}, r is in arcseconds, and the distance d is in parsecs. In the FUV range the absorption coefficient $Q_\nu \sim 1$ (Draine & Lee 1984), and for the typical parameters that we will derive (see Table 3) we obtain $\tau_{\rm FUV} \sim 0.8$. We emphasize that this number refers to the longest path across the clump, so only a small portion at the far side of the clump, with respect to any line of sight, will be only partially thick.

The FUV field emitted by the HH object is intercepted by the flow cavity walls, and a PDR is there formed. A fraction χ_c of the incident FUV field is predicted by PDR models (Tielens & Hollenbach 1985) to be reradiated via the [C II] 158 μm line; our observations allow us to determine (§ 3.3) values of χ_c in very good agreement with model predictions. Since we want to compare the predicted [C II] 158 μm line flux radiated by this PDR with our *ISO*-LWS observations, we are interested in the portion of the flow cavity which is encompassed by the instrument field of view. In other words, we need to estimate the fraction f_c of the $L_{\rm FUV}$ emitted by the HH object which is intercepted by the flow cavity in our LWS beam. The situation is sketched in Figure 7, which serves as reference for the following discussion.

The radius of the cavity is R, and R_b is the radius of the *ISO*-LWS beam. For simplicity, we will assume the HH object lying at the center of our coordinate system as point-like with respect to R. The element solid angle at the cavity wall as seen from the origin is

$$d\Omega = \frac{R\,d\theta\,dz\,\cos\phi}{r^2}\ , \qquad (7)$$

where the cos ϕ factor accounts for the projection, perpendicular to the line of sight from the origin, of the element

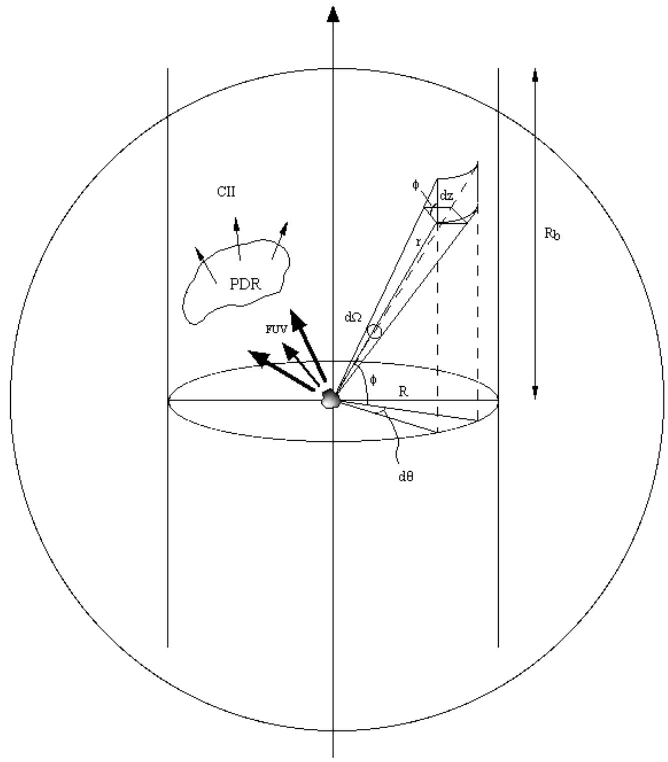

FIG. 7.—Sketch of the proposed scenario for the HH-PDR connection. The HH object is the gray knot at the origin of the coordinate system, and the cylinder represents the cavity excavated by the flow. The big circle indicates the *ISO*-LWS beam.

area of the cavity wall. Expressing z and r as functions of R and ϕ, we obtain

$$d\Omega = \cos\phi\, d\phi\, d\theta\ . \qquad (8)$$

The total solid angle Ω_c under which the HH object sees the internal cavity walls (from $z=-R_b$ to $z=R_b$) is obtained by integrating equation (8) over 2π in $d\theta$ and from $-$arctan (R_b/R) to arctan (R_b/R) in $d\phi$. The FUV field is emitted isotropically, so that

$$f_c = \frac{\Omega_c}{4\pi} = \sin\left(\arctan\frac{R_b}{R}\right). \qquad (9)$$

We can finally write the predicted flux of the [C II] 158 μm line from a system at the distance D as

$$F_{\rm C\,II} = \frac{10^{-7} L_{\rm FUV}\, f_c\, \chi_c}{4\pi D^2}\ {\rm W\ cm^{-2}}\ . \qquad (10)$$

5. DISCUSSION

5.1. *The Herbig-Haro Objects*

To understand which are the critical parameters in our model, it is useful to show a diagnostic diagram that presents the relationship between our two observable quan-

TABLE 3

MODEL INPUTS AND RESULTS FOR HH OBJECTS

Object (1)	χ_c (2)	$r_{\rm HH}$ (arcsec) (3)	R (arcsec) (4)	v_s (km s^{-1}) (5)	$\eta_{\rm ce}$ (6)	FUV (G_0) (7)	n (cm^{-3}) (8)	$\mathscr{R}$ (9)
HH 80........	0.011	5	10	100	2	170	4200	13
HH 81........	0.013	5	10	100	2	180	4500	10
HH 80N......	0.007	5	10	100	2	670	8400	13

tities, $F_{6\,\mathrm{cm}}$ and $F_{\mathrm{C\,II}}$, for various parameter sets. We will first consider the case of the HH objects, where equation (1) holds for the emitted radio continuum flux.

For each grid in Figure 8, the horizontal lines are sites of constant density (n in cm^{-3}) while the vertical lines indicate constant $\mathscr{R} = n/n_0$ compression ratio (density over preshock density). The full-line grid is computed for $v_s = 100$ km s^{-1}, $\eta_{\mathrm{ce}} = 2$, $\chi_c = 0.007$, and $r_{\mathrm{HH}} = 5''$. Decreasing the shock velocity to 70 km s^{-1} shifts the grid to lower radio fluxes (*dashed lines*), while a lower FUV → $\mathrm{C_{II}}$, χ_c, conversion factor brings it down in [C II] 158 μm flux (*dash-dotted lines*; the opposite effect is obtained by raising the η_{ce} enhancement factor). Decreasing the radius of the HH object influences both quantities (*dotted lines*). We find no appreciable effect from the particular choice of the cavity radius R. It is reassuring that for reasonable choices of the model parameters we can reproduce the 6 cm and [C II] 158 μm fluxes observed toward the HH objects. The number of free parameters in our model can be significantly decreased thanks to the available observational evidence. The value of χ_c for each object has been determined using our FIR continuum and [C II] 158 μm measurements (§ 3.3). The radius of the HH objects is taken from the radio maps of MRR93; the objects are clearly resolved, and the full size (after a tentative beam deconvolution) is $\sim 10''$. The value of η_{ce} is computed using its relationship (Dopita et al. 1982) with the degree of excitation measured by the [O III] λ5007/[O I] λ6300 ratio; we use the [O III] λ5007 and [O I] λ6300 line fluxes from HRR to derive values of 2 for the HH objects and 13 for the jet. We adopt shock velocities of 100 km s^{-1} for all HH objects from the measured [O III] 88.3 μm/[N II] 122 μm ratio. Model results are weakly dependent on the cavity radius, for which we adopt a fiducial value of $R = 10''$. We can then vary the plasma density and $\mathscr{R}$ to fit the data, and the results are in columns (7)–(9) of Table 3. For all HH objects we obtain densities which are below 10^4 cm^{-3}, for which $2s \rightarrow 2p$ collisional population would depress the two-photon continuum due to Lyα decay. The presence of a transverse ($\vec{B}_0 \perp \vec{v}_s$) magnetic field limits the compression ratio; we can write (Hollenbach & McKee 1979)

$$B_{0\perp} = 76.7\left(\frac{v_s}{100\ \mathrm{km\ s^{-1}}}\right)\sqrt{\frac{n}{\mathscr{R}^3}}\ \mu\mathrm{G}\ . \tag{11}$$

Using the parameters from Table 3, we see that $B_{0\perp}$ varies from 100 to 200 μG. We ran additional shock models using these large $B_{0\perp}$ values and found that the only way to reproduce the observed line ratios is to assume a preshock ionization fraction ≥ 0.5. This is higher than the higher values (0.2–0.3) found toward several HH jets by Bacciotti & Eislöffel (1999); on the other hand, the HH 80/81 flow is the most powerful in its class and may be peculiar in its ionization fraction as well.

5.2. *The Jet*

As far as the other positions along the jet are concerned, our model has less diagnostic power because of the high number of free parameters in the Reynolds (1986) model for radio emission from ionized jets.

Figure 9 is analogous to Figure 8 for the jet, where grids of models are plotted as a function of density n in cm^{-3} and half-width w_0, in arcseconds, of the jet at its base. While χ_c and η_{ce} are kept fixed to 0.002 (from our observations) and 13 (see above), the jet parameters are essentially free. The full-line grid represents the "pressure-confined" jet in Reynolds terminology, where the density, temperature, and ionization radial gradients of the jet have values $[q_n, q_T, q_x] = [-0.9, -0.6, -0.5]$; in this particular jet the degree of collimation, expressed by a number ϵ which controls the jet's width as a function of radial distance ($w \propto r^{\epsilon}$), is $\epsilon = 0.45$. Another critical parameter, which we cannot independently fix, is the distance from the central source where the jet is injected; the full-line grid in Figure 9 is obtained for $r_0 = 10$ $R_{\odot}$. This model predicts too much radio flux compared to the observations; other classes of standard models in Reynolds study are even less successful. Although of uncertain physical meaning, other combinations of the jet parameters can bring the predicted radio fluxes closer to the values

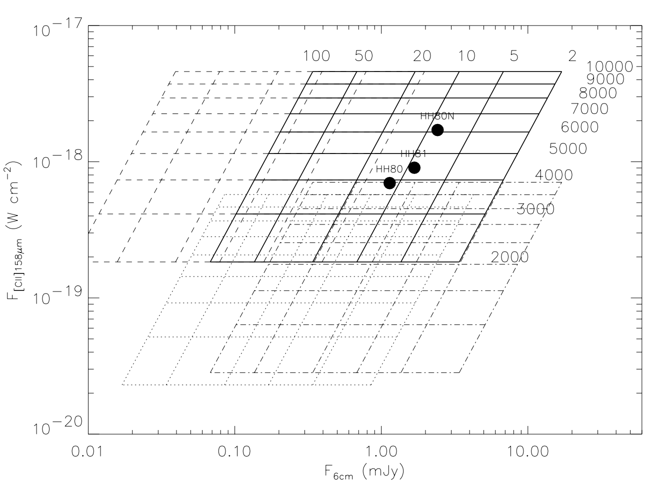

FIG. 8.—[C II] 158 μm line flux as a function of 6 cm radio continuum flux (from eq. [1]) for different choices of HH model parameters. Each grid shows the locus of points of constant density n (*horizontal lines*) and constant $\mathscr{R} = n/n_0$ compression ratio. The full-line grid is computed for $v_s = 100$ km s^{-1}, $\eta_{\mathrm{ce}} = 2$, $\chi_c = 0.007$, and $r_{\mathrm{HH}} = 5''$. The other grids have $v_s = 70$ km s^{-1} (*dashed lines*), $\chi_c = 0.002$ (*dash-dotted lines*), and $r_{\mathrm{HH}} = 2''.5$ (*dotted lines*). The full circles represent the observations.

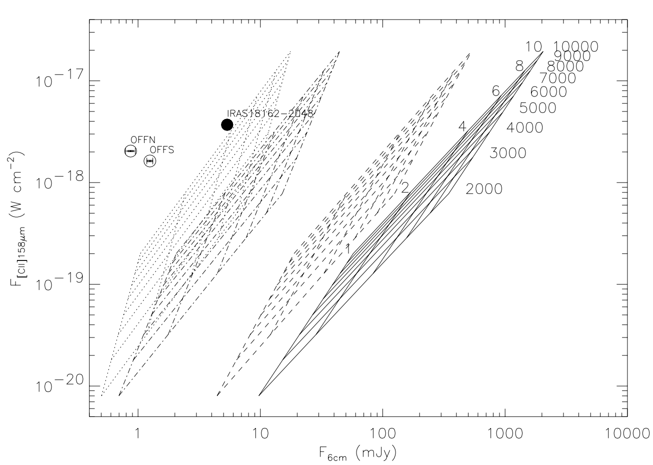

FIG. 9.—[C II] 158 μm line flux as a function of 6 cm radio continuum flux (from Reynolds 1986) for different choices of jet model parameters. Each grid shows the locus of points of constant density n and jet's initial half-width in arcseconds. The full-line grid is computed for $[\epsilon, q_n, q_T, q_x] = [0.45, -0.9, -0.6, -0.5]$. The other grids have $q_T = -1$ (*dashed lines*), $\epsilon = 0.2$ (*dash-dotted lines*), and $q_n = -2$ (*dotted lines*). The circles represent the observations; the open symbols mean an uncertain assignment of the radio flux.

observed along the HH 80/81 jet. Steepening the density gradient to $q_n = -2$ (*dotted grid*) will decrease the radio flux by more than an order of magnitude; a less pronounced effect in the same direction is obtained by decreasing the temperature gradient to, e.g., $q_T = -1$ (*dashed grid*). Providing additional collimation by lowering ϵ down to, e.g., 0.2 (*dash-dotted grid*) will also contribute to a better match between the model and the data. Finally, decreasing the jet-injection distance from the source, r_0, will also work toward lowering the predicted radio flux. Although there is no single set of jet parameters that can fit the data, our model suggests steep density and/or temperature radial gradients along the jet, as well as a very high degree of collimation which is not ruled out by the observations (MRR93). Looking at the shape of the model grids in Figure 9, it seems that a single jet model, i.e., a single model grid, cannot reproduce the $[F_{\rm C\,II}, F_{6\,\rm cm}]$ values of IRAS 18162−2048 and the two OFF positions. This is not due to the misalignment between the observed OFF positions and the jet axis. A better alignment would not have changed the radio flux (which we arbitrarily assigned based on the 6 cm map of MRR93); likewise, a half-LWS beam shift in the *ISO* observed positions would certainly not result in a 1 order of magnitude decrease of the [C II] 158 μm line fluxes, as required to bring the OFF positions onto the model grid in Figure 9. Rather, it is plausible that the central (brighter) portion of the jet considerably contributes to the FUV irradiation of the flow cavities at the two OFF positions. This would indeed correspond to increasing the assigned radio flux to the two OFF positions in Figure 9.

5.3. *The $F_{\rm C\,II}$-$F_{6\,\rm cm}$ Relationship*

Although it was one of the motivations to develop our model, one of the consequences of the model is that an $F_{\rm C\,II}$-$F_{6\,\rm cm}$ relationship is difficult to justify. The radio flux has a different origin in the HH objects and the jet; there is a priori no reason why IRAS 18162−2048 (where we model the radio flux as coming from a jet) should line up with the three HH objects (where we model the radio flux as coming from the postshock region) in Figure 6. The relative position of the HH objects themselves is also a priori depending on a high number of free parameters. Based on four points only, we must then conclude that the $F_{\rm C\,II}$-$F_{6\,\rm cm}$ relationship in Figure 6 appears to be fortuitous. However, we will check for similar occurrences in other HH/jet systems where [C II] 158 μm data are available and where the densities are low enough ($n \leq 10^4$ cm^{-3}) that a shock/jet ↔ PDR connection can be expected.

6. CONCLUSIONS

We have performed a FIR spectroscopic study of the HH 80/81 system. Line ratio analysis confirms for the first time the Herbig-Haro nature of the nebulosity HH 80N, which probably represents the head of the counterflow to HH 80 and 81. We reveal shock velocities of the order of 100 km s^{-1} in correspondence with the HH objects, while lower excitation conditions appear to be present elsewhere along the radio jet. A comparison with proper motion velocities in excess of 600 km s^{-1} indicates that the shocks arise at the interface between two fast-moving flows.

Besides shock-excited emission, an important PDR contribution is present all along the bipolar flow, where densities below 10^4 cm^{-3} are also diagnosed. Using a simple model, we have provided quantitative arguments supporting the idea that the FUV field radiated by the ionized material of the recombination regions in the HH objects and of the jet emanating from IRAS 18162−2048 is able to induce the formation of a PDR in the immediately surrounding medium (i.e., the flow cavity walls). This would provide further evidence that the jet/HH own radiation field affects its surrounding medium in a measurable way. Attempts to model the chemistry of outflows should not ignore the influence of the radiation field of the shocks responsible for the acceleration of the outflow itself.

We thank Luis Felipe Rodríguez for kindly making available to us his 6 cm VLA map of the HH 80/81 region. We also thank the referee, Chris Davis, for his careful reading of the manuscript. The *ISO* Spectral Analysis Package (ISAP) is a joint development by the LWS and SWS Instrument Teams and Data Centers. Contributing institutes are Centre d'Etude Spatiale des Rayonnements (France), Institute d'Astrophysique Spatiale (France), Infrared Processing and Analysis Center (United States), Max-Planck-Institut für extraterrestrische Physik (Germany), Rutherford Appleton Laboratories (United Kingdom), and the Space Research Organization (Netherlands).

REFERENCES

Aspin, C., et al. 1994, A&A, 292, L9
Aspin, C., & Geballe, T. R. 1992, A&A, 266, 219
Bacciotti, F., & Eislöffel, J. 1999, A&A, 342, 717
Beck-Winchatz, B., Böhm, K. H., & Noriega-Crespo, A. 1996, AJ, 111, 346
Binette, L., Dopita, M. A., & Tuohy, I. R. 1985, ApJ, 297, 476
Churchwell, E. 1999, in The Origin of Stars and Planetary Systems, ed. C. J. Lada & N. D. Kylafis (NATO ASI Ser. C, 540; Dordrecht: Kluwer), 515
Clegg, P. E., et al. 1996, A&A, 315, L38
Curiel, S., Cantó, J., & Rodríguez, L. F. 1987, Rev. Mexicana Astron. Astrofis., 14, 595
Davis, C. J., Dent, W. R. F., & Burnell, S. J. Bell. 1990, MNRAS, 244, 173
de Graauw, T., et al. 1996, A&A, 315, L49
Dopita, M. A., Binette, L., & Schwartz, R. D. 1982, ApJ, 261, 183
Draine, B. T. 1980, ApJ, 241, 1021
Draine, B. T., & Lee, H. M. 1984, ApJ, 285, 89
Eislöffel, J., Mundt, R., & Böhm, K. H. 1994, AJ, 108, 1042
Emerson, D. 1996, Interpreting Astronomical Spectra (Chichester: Wiley)
Girart, J. M., Estalella, R., & Ho, P. T. P. 1998, ApJ, 495, L59
Girart, J. M., et al. 1994, ApJ, 435, L145
Habing, H. J. 1968, Bull. Astron. Inst. Netherlands, 19, 421
Hartigan, P., Raymond, J., & Hartmann, L. 1987, ApJ, 316, 323
Hartmann, L. 1998, Accretion Processes in Star Formation (Cambridge: Cambridge Univ. Press), 13
Heathcote, S., Reipurth, B., & Raga, A. 1998, AJ, 116, 1940
Herbig, G. H., & Jones, B. F. 1981, AJ, 86, 1232
Hollenbach, D., & McKee, C. F. 1979, ApJS, 41, 555
Hollenbach, D., & McKee, C. F. 1989, ApJ, 342, 306
Hummer, D. G., & Seaton, M. J. 1963, MNRAS, 125, 437
Kaufman, M. J., & Neufeld, D. A. 1996, ApJ, 456, 611
Kessler, M. F., et al. 1996, A&A, 315, L27
Martí, J., Rodríguez, L. F., & Reipurth, B. 1993, ApJ, 416, 208 (MRR93)
———. 1995, ApJ, 449, 184
———. 1998, ApJ, 502, 337
Miller, G. E., & Scalo, J. M. 1979, ApJS, 41, 513
Molinari, S., Brand, J., Cesaroni, R., & Palla, F. 2000, A&A, 355, 617
Noriega-Crespo, A., Böhm, K. H., & Raga, A. C. 1990, AJ, 99, 1918
Noriega-Crespo, A., Garnavich, P. M., Curiel, S., Raga, A. C., & Ayala, S. 1997, ApJ, 486, L55
Nussbaumer, H., & Schmutz, W. 1984, A&A, 138, 495
Ogura, K. 1995, ApJ, 450, L23
Pequignot, D. 1986 in Workshop on Model Nebulae, ed. D. Péquignot (Paris: Observatoire de Paris), 363
Poetzel, R., Mundt, R., & Ray, T. P. 1989, A&A, 224, L13
Pravdo, S. H., Rodríguez, L. F., Curiel, S., Cantó, J., Torrelles, J. M., Becker, R. H., & Sellgren, K. 1985, ApJ, 293, L35
Raga, A. C., Binette, L., Canto, J., & Calvet, N. 1990, ApJ, 364, 601
Raga, A. C., & Böhm, K. H. 1986, ApJ, 308, 829

Raga, A. C., & Williams, D. A. 2000, A&A, 358, 701
Reipurth, B., & Graham, J. A. 1988, A&A, 202, 219
Reipurth, B., & Heathcote, S. 1997 in IAU Symp. 182, Herbig-Haro Flows and the Birth of Low-Mass Stars, ed. B. Reipurth & C. Bertout (Dordrecht: Kluwer), 3
Reynolds, S. P. 1986, ApJ, 304, 713
Rodríguez, L. F., Curiel, S., Ho, T. P., Torrelles, J. M., & Cantó, J. 1990, ApJ, 352, 645
Rodríguez, L. F., Moran, J. M., Ho, P. T. P., & Gottlieb, E. W. 1980, ApJ, 235, 845
Rodríguez, L. F., & Reipurth, B. 1989, Rev. Mexicana Astron. Astrofis., 17, 59
Shepherd, D. S., & Churchwell, E. 1996, ApJ, 472, 225
Shull, J. M., & McKee, C. F. 1979, ApJ, 227, 131
Stone, J. M., & Norman, M. L. 1993, ApJ, 413, 210
Tielens, A. G. G. M., & Hollenbach, D. 1985, ApJ, 291, 722
Torrelles, J. M., et al. 1992, ApJ, 396, L95
———. 1993, ApJ, 417, 655
Wolfire, M. G., & Königl, A. 1993, ApJ, 415, 204